J Mater Sci (2011) 46:1446–1454
DOI 10.1007/s10853-010-4943-0

Densification and microstructural evolution during laser sintering of A356/SiC composite powders

A. Simchi · D. Godlinski

Received: 15 April 2010 / Accepted: 21 September 2010 / Published online: 7 October 2010

Abstract This article reports experimental results on laser sintering of A356 aluminum alloy and A356/SiC composite powders. Effects of scan rate, sintering atmosphere, hatch spacing, and SiC volume fraction (up to 20%), and particle size (7 and 17 μm) on the densification were studied. The phase formation and microstructural development were analyzed by X-ray diffraction (XRD) and scanning electron microscopy (SEM) coupled with energy-dispersive X-ray spectroscopy (EDS). Laser sintering under argon atmosphere exhibited higher densification compared to nitrogen. A faster sintering kinetics was observed as the scan rate decreased. Except at a low SiC content (5 vol%), the composite powders exhibited lower densification kinetics. The densification was improved when finer SiC particles were utilized. Microstructural studies revealed directional solidification of aluminum melt to form columnar grains with inter-columnar silicon precipitates. In the presence of SiC particles, aluminum melt reacted with the ceramic particles to form Al_4SiC_4 plates.

A. Simchi (✉)
Department of Materials Science and Engineering,
Sharif University of Technology, Azadi Avenue,
P.O. Box 11365-9466, 14588 Tehran, Iran
e-mail: simchi@sharif.edu

A. Simchi
Institute for Nanoscience and Nanotechnology (INST),
Sharif University of Technology, Azadi Avenue,
P.O. Box 11365-9466, 14588 Tehran, Iran

D. Godlinski
Fraunhofer Institute for Manufacturing Technology
and Advanced Materials IFAM, Wiener Str. 12,
28359 Bremen, Germany

Introduction

Solid freeform fabrication (SFF) techniques enable quick production of intricate-shaped parts directly from CAD data. During the last two decades, various processing techniques have been developed and being used in commercial scale. Among diverse procedures, powder-based technologies can be used for the fabrication of functional prototypes and tools with no or limited subsequent post-processing steps. When the process is combined with the advantages of laser technology, the procedure becomes particularly useful for quick fabrication of complex-shaped parts with high materials flexibility. Laser-engineered net-shaping (LENS®) and laser sintering are two successful examples which have attracted significant attention in the last decade. While in the former, powder particles are injected into a molten pool formed by a high-intensity laser, in the latter a laser beam partially melts row by row loose packed powder in a bed to join (sinter) the particles. Since a powder bed is used in the laser sintering process, full densification is only achievable at high laser-energy input in order to induce complete melting of the powder particles. Here, the chemical composition of the material and laser processing parameters are of crucial importance. It has been reported elsewhere [1, 2] that the density versus the input energy approaches a plateau, upon which densification is restricted by cracking of the sintered-layers.

In the last decade, much research has been devoted on laser sintering of metals and alloys [3–7]. Recently, studies have focused on laser sintering of composite powders [8–14]. Nevertheless, the application of SFF techniques on the development of composite parts is still in the infant stage [14]. Particularly, fabrication of particulate-reinforced aluminum matrix composites by the laser sintering process is notified very limitedly. Vaucher et al. [15] could build few layers by laser sintering of Al/SiC powder mixture. The high oxygen affinity of aluminum, low laser-absorption rate of the metal (especially for CO_2 laser), and relatively low wettability of SiC particles with aluminum melt make the process very difficult [16]. Due to wide industrial usage of aluminum matrix composites as a result of their excellent combination of physical and mechanical properties, laser sintering could be a very promising and attractive manufacturing technique, enabling the rapid fabrication of complex-shaped parts. The aim of the present work is twofold. First, the effect of processing parameters (scan rate, atmosphere, and hatch spacing) on the densification of A356 alloy was studied. The highest available laser power (200 W) and lowest possible layer thickness (0.1 mm at which the powder deposition was feasible) were utilized in order to ensure maximum sintering kinetics. The microstructure of the laser-sintered parts was examined and described based on the solidification of aluminum melt under laser irradiation. Second, SiC particles with two different sizes at various volume fractions (5, 10, 15, and 20%) were mixed with the aluminum alloy and the densification of the composite powders were studied. The phase formation and microstructural development during laser sintering of A356/SiC composite powders were also evaluated.

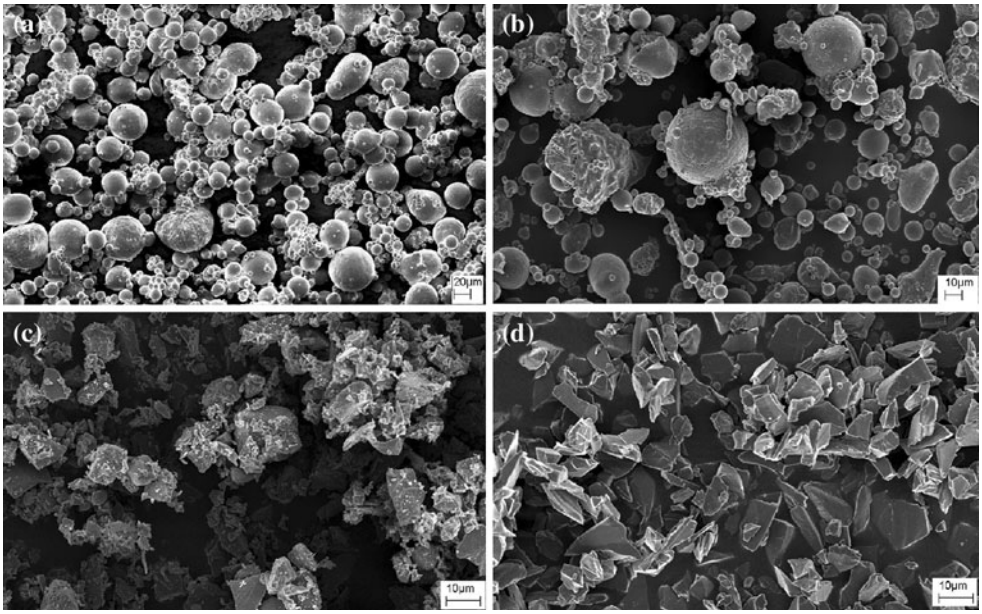

Fig. 1 SEM micrographs showing the morphology of **a** Al, **b** Al–10 wt%Mg, **c** Si, and **d** SiC particles

Table 1 Density (%theoretical) of A356 alloy and A356/SiC composites sintered at various laser scan rates under argon atmosphere

Material	Particle size (μm)	vol% SiC	Tap density	Laser-sintered density at scan rate of					
				75	100	125	150	175	200
A356 alloy	–	0	64.6	82.4	79.2	78.2	74.6	73.9	72.8
A356/SiC composite	7	5	62.9	79.0	80.4	79.3	78.3	77.8	77.3
		10	59.3	[a]	70.6	71.1	69.6	69.4	68.0
		15	58.7	[a]	72.0	68.2	68.4	66.9	66.6
		20	58.1	[a]	70.1	69.8	68.3	69.3	66.9
	17	5	63.1	65.7	68.7	67.9	66.2	64.6	62.6
		10	62.4	[a]	55.9	55.9	57.6	56.3	54.5
		15	61.8	[a]	55.0	55.4	55.9	54.9	52.7
		20	61.3	[a]	54.6	54.6	53.0	52.4	47.7

The laser intensity was 1.6 kW/mm^2

[a] Sound part could not be built

Experimental procedure

Gas atomized aluminum powder with an average particle size of 44 μm and spherical shape was supplied by TLS Technik GmbH & Co (Bitterfeld, Germany) (Fig. 1a). To prepare A356 alloy with nominal composition of Al–7Si–0.3Mg (wt%), aluminum–magnesium master alloy and silicon powders were added to the aluminum powder in a proper mass fraction and mixed in a 2F Turbula shaker/mixer (Willy A. Bachofen AG, Basel, Switzerland) for 20 min. The master alloy was gas-atomized powder with an average particle size of 35 μm with spherical shape (Fig. 1b). The silicon particles had irregular shape with an average size of 7 μm (Fig. 1c) and supplied by Saint-Gobain (Duisburg, Germany). Two SiC powders of sizes of 7 and 17 μm (H.C. Stark GmbH, Goslar, Germany) were utilized. The morphology of the particles is shown in Fig. 1d. The composite powders were prepared by blending of the aluminum-alloy powder mixture with SiC particles in the Turbula mixer 30 min. The volume fraction of ceramic particles was 5, 10, 15, and 20%. The tap density (MPFI Standard 46; ISO 3953; ASTM B 527) of the examined powder mixtures was reported in Table 1. The density of the aluminum-alloy powder mixture was ~64% of the pore-free density and varied dependent on the volume fraction and size of SiC particles.

The laser sintering was performed using a commercial M250X$^{\text{tend}}$ machine (Electro Optical Systems GmbH, Munich, Germany) by a continuous wave CO_2 laser at the output powder of 200 W. A uniform powder layer (0.1 mm thickness) was deposited on a sand blasted aluminum plate (HASCO, Hasenclever GmbH & Co KG, Germany) using a moving wiper. The laser sintering was performed under an argon or nitrogen atmosphere. The scan rate was varied between 50 and 225 mm/s. The examined hatch spacing was 0.2 mm and 0.3 mm. The powder bed temperature was kept constant at 80 °C. The test part was a cylindrical specimen with a diameter of 15 mm and height of 5 mm. The CAD file of the specimen was built using ProEngineer software and sliced to 0.1 mm layers to generate a stereolithography (STL) file. Beam compensation was utilized to compensate the focus diameter of the laser beam to ensure the correct part geometry. The deviation of the geometry of the cylindrical samples from the target geometry was about 1–2%.

After laser sintering, the cylindrical specimens were removed from the aluminum plate and cleaned by air flashing. The sintered density was determined by volumetric method as well as by water displacement method according to ISO Standard 5017. Variance analysis indicated that the error of measurement for different specimens built in a same condition is less than 1% pore-free density. The upper surfaces of the laser-sintered specimens were observed by scanning electron microscopy (LEO GEMINI 1530, ZEISS, Germany) to study the densification mechanism and the role of processing parameters mentioned above. The phase analysis was performed by X-ray diffractometry (XRD, Siemens AG, Germany) with Cu K_α radiation. A step size of 0.02° with a data acquisition of five per second was recorded. Samples for microstructural

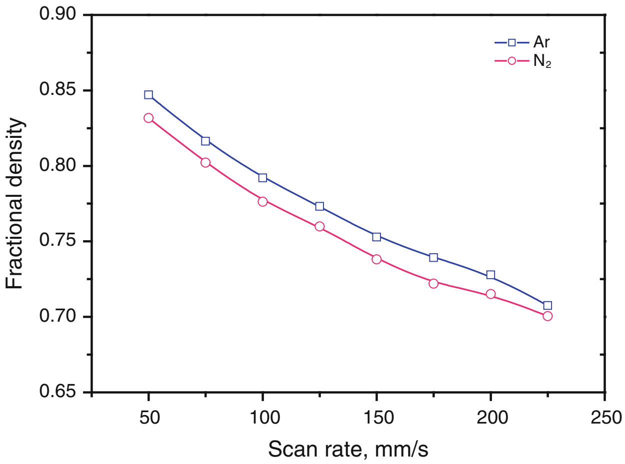

Fig. 2 Density of A356 specimens prepared by laser sintering under argon and nitrogen atmospheres

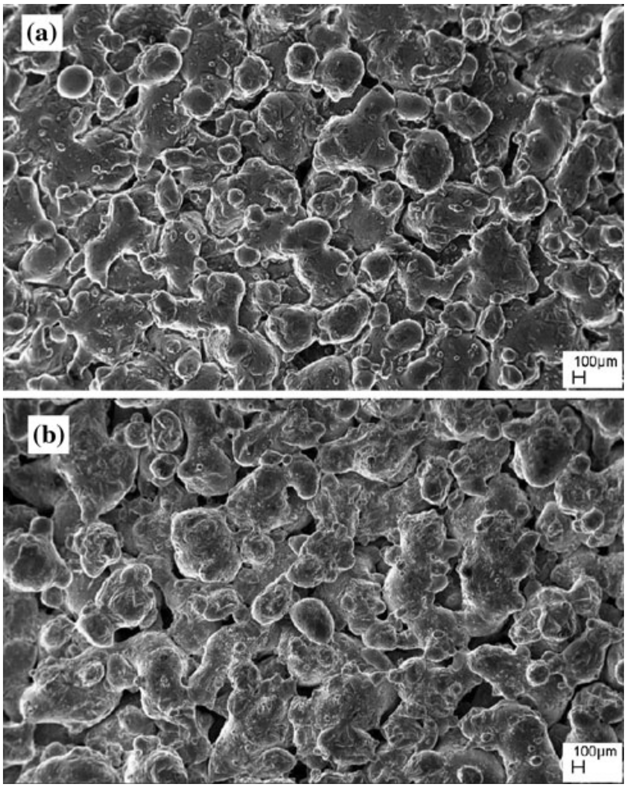

Fig. 3 SEM micrographs showing the surface morphologies of laser-sintered A356 alloy prepared at scan rate of 100 mm/s under **a** argon and **b** nitrogen atmosphere

studies were prepared by sectioning of the cylindrical specimens parallel to the building direction, i.e. along the thickness and perpendicular to the line scanning, followed by grinding on emery papers and mechanical polishing. Fine polishing/etching was performed by OPS solutions (Struers, Copenhagen, Denmark). The microstructure of the laser-sintered parts was studied by optical microscopy and SEM coupled with energy-dispersive X-ray spectroscopy (EDS). To reveal the structure of phases in the laser-sintered specimens under SEM, the aluminum matrix was removed by electrochemical etching in a solution of 33 vol% HNO_3 and 67 vol% H_2O. The voltage and current were 10–15 dc V and 5–10 A, respectively.

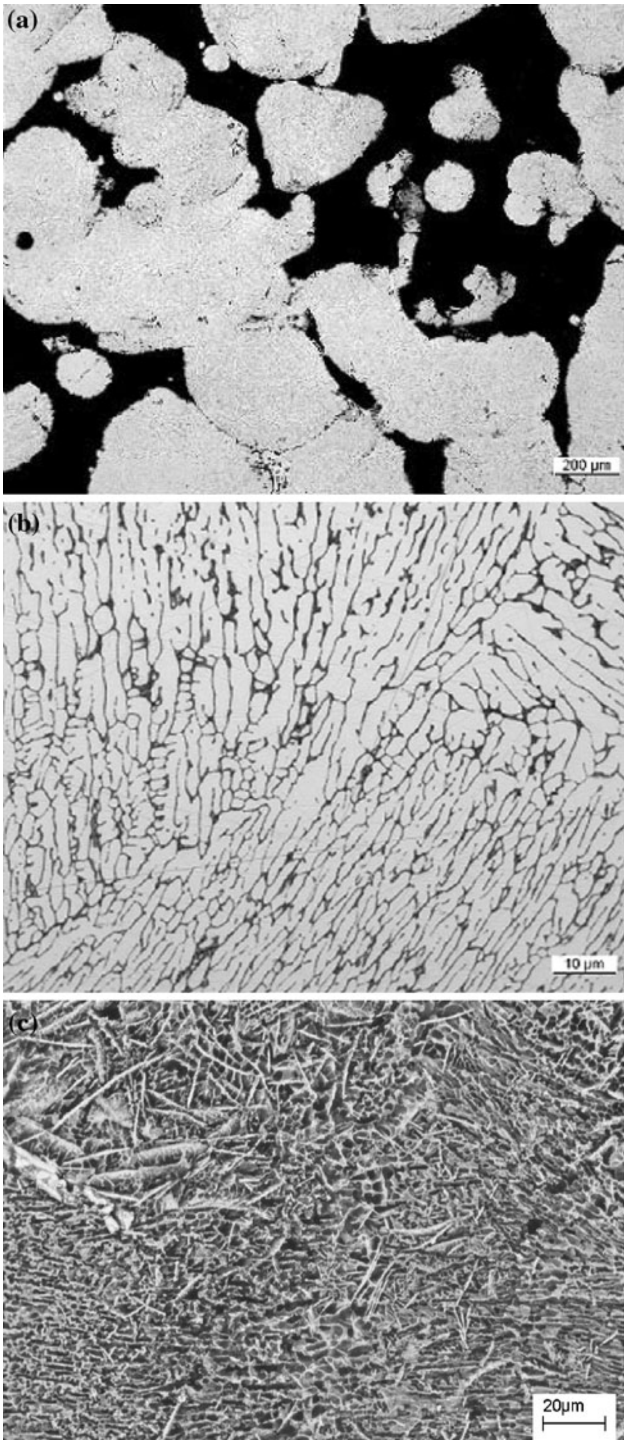

Fig. 4 **a**, **b** Optical micrographs show the microstructure of A356 alloy sintered under argon atmosphere at laser scan rate of 100 mm/s. **c** SEM picture shows the microstructure after electrochemical etching

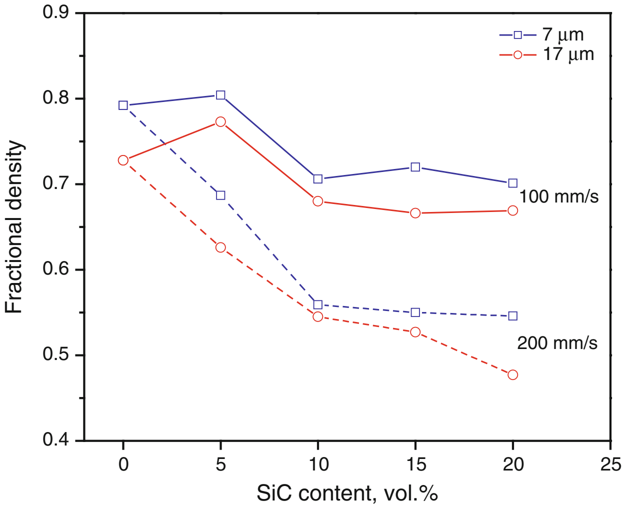

Fig. 5 Density of A356/SiC composite powders as a function of SiC volume fraction and particle size at two laser scan rates of 100 mm/s (*solid lines*) and 200 mm/s (*dash lines*) with hatch spacing of 0.3 mm under argon atmosphere

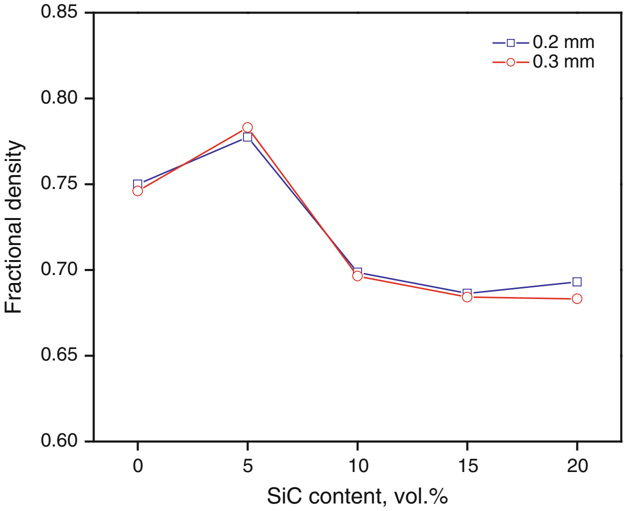

Fig. 6 Effect of hatch spacing on the density of composite powders prepared by laser sintering of A356/SiC (7 µm) under argon atmosphere

Results

The first runs were performed on A356 powder to determine the effect of scan rate and sintering atmosphere on the sintering kinetics. Figure 2 shows the laser-sintered density of the aluminum alloy. The density decreased with increasing the scan rate while higher density was obtained under the argon atmosphere. Figure 3 shows the surface morphologies of the sintered parts at scan rate of 100 mm/s. The surface consisted of metal agglomerates and interconnected pores. Larger agglomerates and higher surface roughness were obtained by processing under nitrogen atmosphere. Figure 4 shows the microstructure of the sintered specimen under argon atmosphere. The formation of large metal agglomerates with interconnected pores is visible in Fig. 4a. Figure 4b shows the microstructure of the aluminum alloy, revealing columnar grains with fine silicon inter-columnar precipitates, and a small portion of equiaxed grains. Figure 4c illustrates the morphology of the silicon precipitates extracted by electrochemical etching using a HNO_3 solution.

When SiC particles were added to the aluminum alloy significant changes in the densification and microstructural features were realized. Table 1 reports the density of sintered specimens at various scan rates. Since better densification and smaller agglomerates were obtained under the argon atmosphere, laser sintering of the composite powders were performed under Ar. The data show a great effect of SiC volume fraction and particle size on the sintering kinetics of A356 powder under laser irradiation. For instance, the sintered density as a function of SiC content at two different sizes and scan rates is shown in Fig. 5. In agreement with unreinforced A356 alloy, increasing the scan rate led to a slower sintering kinetics. The results also showed that finer ceramic particles yielded higher sintering rates. Except for low SiC volume fraction of 5%, the densification was lower when the amount of SiC particles increased. As shown in Fig. 6, this trend holds true by varying the hatch spacing although the effect was marginal.

Figure 7 shows the surface morphologies of laser-sintered specimens containing 10% and 20% SiC particles of two different sizes. The morphologies exhibit typical features of laser-sintered A356 alloy that are formation of metallic agglomerates and interconnected pores. The size of the aggregates ranges between 200 and 400 μm and they are connected together by small necks. The surface roughness and size of the agglomerates and interconnected

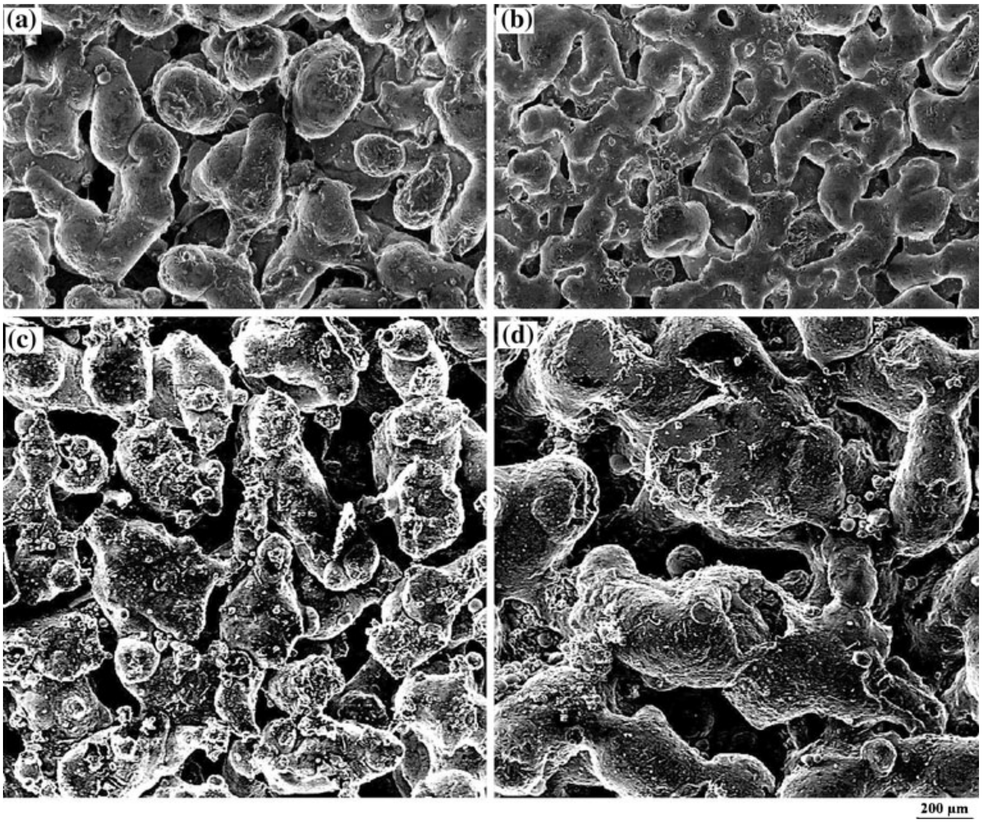

Fig. 7 SEM micrographs showing the surface morphologies of A356/SiC composite laser sintered under argon atmosphere at scan rate of 100 mm/s and hatch spacing of 0.3 mm. **a** 10 vol% SiC (7 μm), **b** 20 vol% SiC (7 μm), **c** 10 vol% SiC (17 μm), **d** 20 vol% SiC (17 μm)

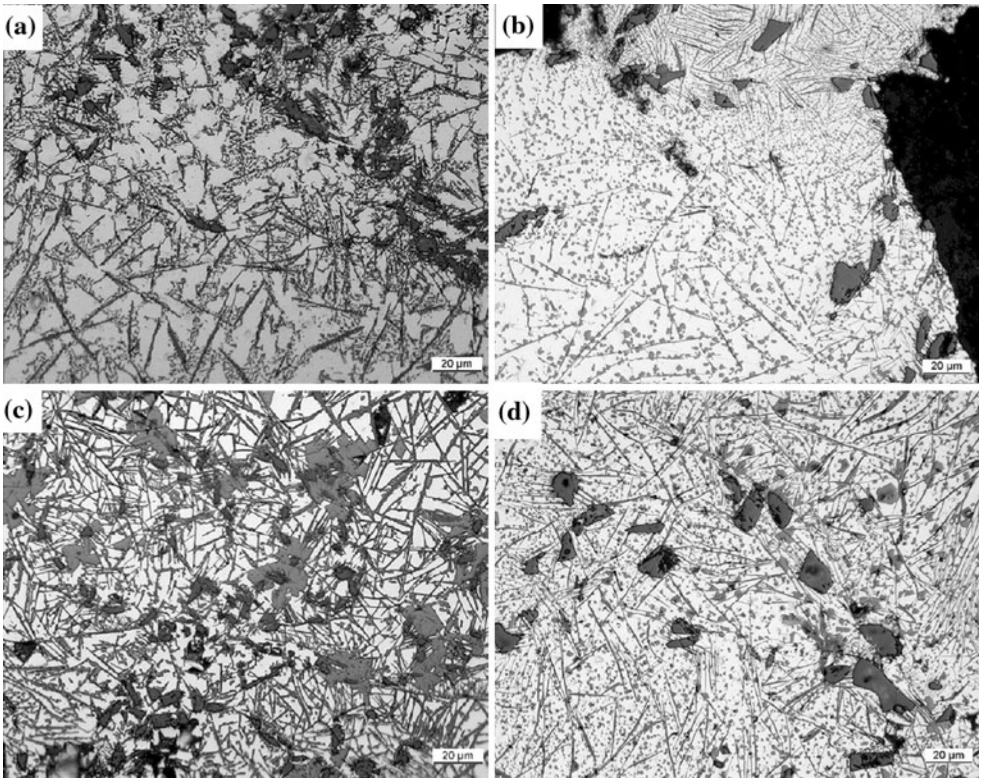

Fig. 8 Optical micrographs showing the microstructure of laser-sintered A356/SiC composites prepared under argon atmosphere at scan rate of 100 mm/s and hatch spacing of 0.3 mm. **a** 10 vol% SiC (7 μm), **b** 10 vol% SiC (17 μm); **c** 20 vol% SiC (7 μm), **d** 20 vol% SiC (17 μm)

pores were found to decrease with increasing SiC content. The agglomerates became larger as the SiC particles size deceased. Metallographic studies revealed that the microstructure of A356/SiC composites consisted of aluminum, pro-eutectic silicon, and three-dimensional plate-like precipitates (Fig. 8). XRD patterns of the laser-sintered specimens showed that the precipitates are Al_4SiC_4 (Fig. 9), determining that a reaction between the aluminum melt and silicon carbide occurred at temperatures >1670 K [17]. No remarkable influence of SiC particle size on the XRD patterns could be noticed. Although a low step size (0.02°) was utilized for the XRD analysis, the characteristic peaks of aluminum oxide were not detected (in contrast to the results of Vaucher et al. [15] and Gasci et al. [18]) by considering the limitation of XRD in detecting phases in low volume fractions. The microstructural studies revealed that the amount of silicon particles and the ternary carbide increased with increasing the SiC content. Moreover, ceramic clusters were formed when finer SiC particles were utilized while the coarse particles were more dispersed.

Discussion

The formation of relatively large metal agglomerates and interconnected pores reveals that the aluminum alloy powder was melted under the laser energy (Figs. 3, 4a). The microstructure of the sintered specimens also showed directional solidification of the superheated melt to form fine columnar grain structure with inter-columnar precipitates (Fig. 4b, c). The configuration of columnar and equiaxed grains points out the effect of crystallographic orientation, i.e. for metals with cubic crystal structure dendrite tips grow preferentially in $\langle 100 \rangle$ cubic directions [19] relative to the local heat-flow, i.e. building direction. Furthermore, the competition of grains during growth led to formation of coarser grains at the upper regions. We have found that slightly higher density is obtained by processing A356 powder under argon atmosphere at various scan rates (Fig. 2). Similar results have been reported for iron powders previously [2]. It is suggested that the purity of the sintering atmospheres and the possible gas–liquid reaction(s) during laser sintering played role on the densification. In other words, the higher purity of the used argon atmosphere and its neutrality to the aluminum melt would affect the densification process as similar to what observed for iron. Intensifying the laser energy input by decreasing the scan rate resulted in a higher working temperature, which consequently lowers the melt viscosity and surface tension; hence, the melt flow to fill the pores is easier and the melt stability is higher. Finally, the inter-agglomerate pores decrease and higher density is attained.

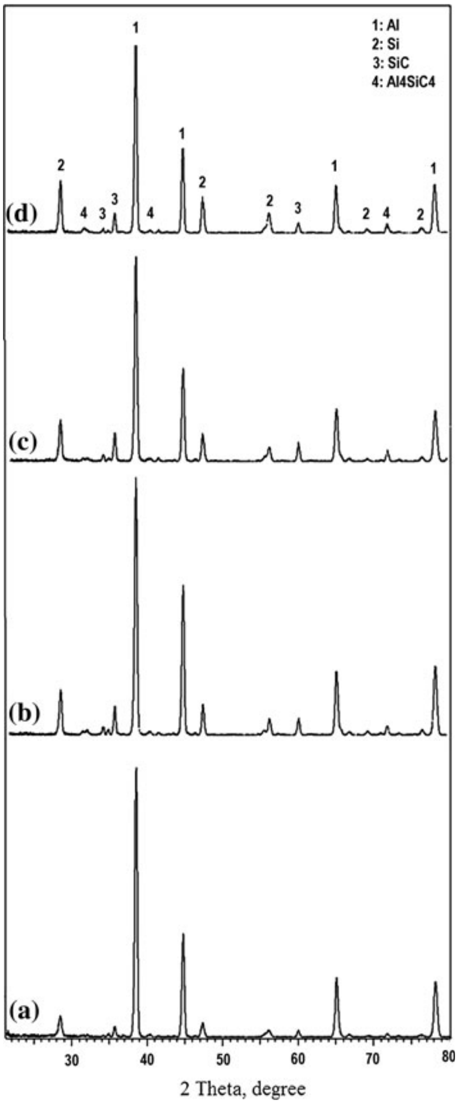

Fig. 9 XRD patterns of laser-sintered A356/SiC composite powders containing different amounts of SiC particles with an average size of 17 µm: (*a*) 5% (*b*) 10%; (*c*) 15%; (*d*) 20%

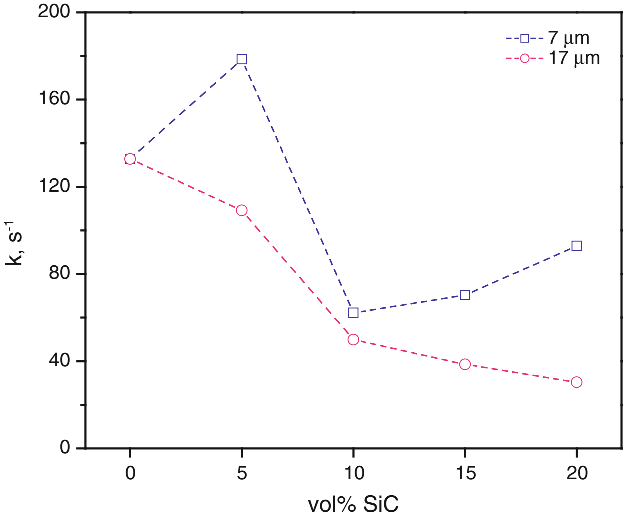

Fig. 10 Sintering rate of A356/SiC composite powder as a function of SiC volume fractions of two sizes. The powders were laser-sintered under argon at various scan rates at a constant hatch spacing of 0.3 mm

When SiC particles were mixed with A356 powder and subjected to laser sintering, the sintering kinetics and the microstructural features were altered. Figure 10 shows the sintering rate constant (k) as a function of SiC volume fraction for two sizes. The constant was calculated based on the first-order sintering model proposed for densification of metal powders [1, 2]. Except A356/5vol% SiC (7 µm) composite, a lower sintering rate was obtained for the composite powders compared to the base alloy. A faster sintering rate was attained for powders containing finer ceramic particles. Microstructural studies (Fig. 8) revealed that as similar to A356 alloy, the aluminum alloy powder was melted during laser sintering while the SiC particles were almost unaffected. Therefore, the sintering mechanism can be considered similar to liquid phase sintering ($\mathrm{Al}_{(l)} + \mathrm{SiC}_{(s)}$). By increasing the SiC volume fraction, the amount of solid phase increased; hence, the higher viscosity of the mixture decreased the densification. The lower powder-bed density (see Table 1) is also responsible for the lower final density. The higher effective surface area of finer particles improves the laser absorption efficiency because of high absorption capacity of the ceramic particles to CO_2 laser beam [20]. Therefore, the working temperature should be higher when using finer particles and as a result a faster sintering kinetics is expected. When the amount of SiC particles is low (<5%), the effect of solid phase on the viscosity of the molten metal is marginal, so that the higher absorption coefficient of the powder bed increased the sintering rate. Studies of the surface morphologies of laser-sintered specimens (Fig. 7) revealed that the presence of SiC particles affected the “balling effect” as they resulted in the formation of smaller metal agglomerates. It seems that the ceramic particles improved the stability of the molten track formed during line scanning. It is known that a cylindrical molten track becomes unstable when the wavelength of sinusoidal fluctuations (λ) is greater than the cylinder circumference (πD). The diameter of the molten cylinder increases when ceramic particles exist, owing to higher effective absorbability of the powder bed which leads to a higher working temperature. As a result, it is more difficult for the cylinder to break up to spheres and eventually more continuous surface (lower surface roughness) is attained. Obviously, that effect was more pronounced at higher SiC content, particularly when fine particles (higher surface area) were used. After solidification of the molten track, the microstructure of agglomerates consisted of aluminum matrix,

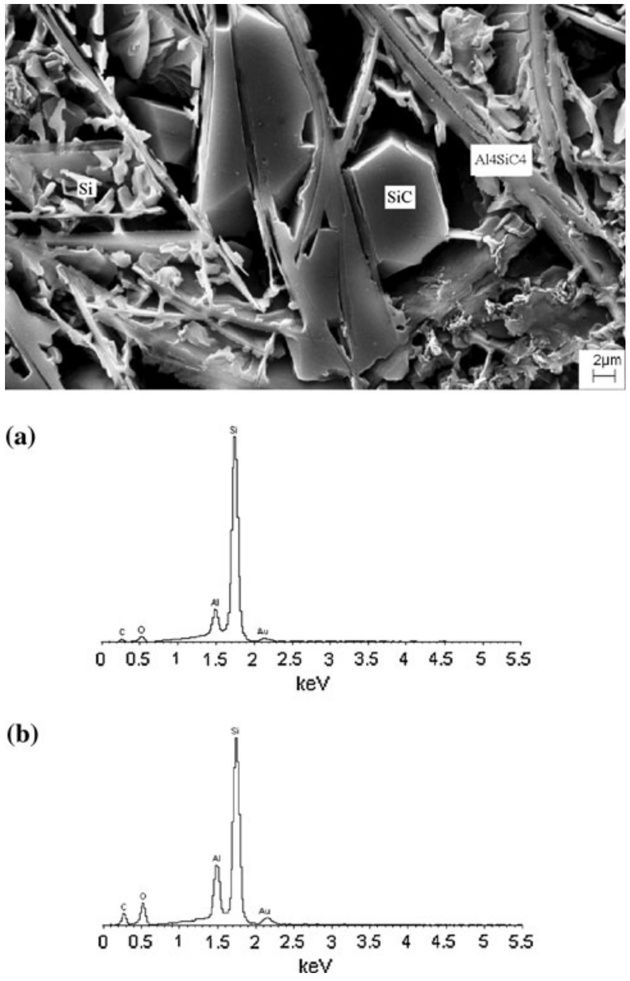

Fig. 11 SEM micrograph showing the microstructure of A356/20%SiC (7 μm) after electrochemical etching to remove the aluminum matrix. The EDX spectra are for **a** silicon and **b** the ternary carbide phase

silicon carbide, silicon, and ternary carbide (Fig. 8). To better reveal the phases, electrochemical etching was utilized. Figure 11 shows a SEM micrograph and EDS spectra of the silicon and ternary carbide phases. The Au and O peak are from the gold coating and surface oxidation by the chemical etching, respectively. It is seen that the plate-like ternary carbide was formed adjacent to the silicon carbide particles, revealing the reaction between the aluminum melt and silicon carbide

$$4\mathrm{Al}_{(l)} + 4\mathrm{SiC}_{(s)} \rightarrow \mathrm{Al}_4\mathrm{SiC}_{4(s)} + 3\mathrm{Si} \qquad T > 1670\,\mathrm{K} \qquad (1)$$

Al_4SiC_4 initially forms as faceted platelets at the interface between SiC and the liquid, and Si dissolves in the liquid and eventually the Si-rich hypereutectic liquid is solidified to pro-eutectic silicon and α-Al + Si eutectic [21]. It should be noted that the equilibrium dissolved Si in the aluminum melt in the presence of SiC can exceed the eutectic composition at temperatures above 1273 K [22]. Therefore, it is suggestible that under the laser intensity, especially at high volume fractions of SiC, the Al–Si melt with super high Si content was crystallized to form eutectic and single Si phase.

Conclusions

The densification and microstructural formation during laser sintering of A356 alloy and A356/SiC composite powders were investigated. The effect of the processing parameters including scan rate, sintering atmosphere, hatch spacing, and the reinforcement volume fraction and particle size was studied. The results are summarized as follows:

- The microstructure of laser-sintered A356 alloy consisted of columnar aluminum grains and fine inter-columnar silicon. The densification rate was slightly higher when sintering was performed under argon atmosphere. Slower sintering kinetics was obtained by increasing the scan rate.
- The addition of SiC particles reduced the sintering rate of A356 alloy except at low volume fraction (5%) of the fine particles. Lower density was obtained as the scan rate increased while the effect of hatch spacing was marginal.
- Lower sintering kinetics was obtained at higher SiC volume fractions.
- Increasing the SiC particle size yielded lower densification.
- The ceramic particles increased the melt stability and induced more continuous surface morphology with smaller inter-agglomerate pores.
- The microstructure of the sintered composites consisted of α-Al, Si, SiC, and Al_4SiC_4 phases. The plate-like ternary carbide phase was formed due to the reaction of the aluminum alloy with silicon carbide at $T > 1670$ K.

Acknowledgement Partial funding of this work by the European Commission within the Network of Excellence “Knowledge-based multicomponent materials for durable and safe performance” (KMM-NoE) is acknowledged.

References

1. Simchi A (2006) Mater Sci Eng 428A:148
2. Simchi A (2004) Metall Mater Trans 35B:937
3. Traini T, Mangano C, Sammons RL, Mangano F, Macchi A, Piattelli A (2008) Dent Mater 24:1525
4. Gu DD, Shen YF (2006) Metall Mater Trans 37B:967
5. Fischer P, Romano V, Weber HP, Kolossov S (2004) Thin Solid Films 453–454:139

6. Kruth JP, Froyen L, Rombouts M, Van Vaerenbergh J, Mercells P (2003) CIRP Ann Manuf Technol 52:139
7. Simchi A, Petzoldt F, Pohl H (2001) Int J Powder Metall 37:49
8. Liu DM, Si TZ, Wang CC, Zhang QA (2007) Scripta Mater 57:389
9. Gu DD, Shen YF (2006) Mater Sci Eng A435–436:54
10. Gåård A, Krakhmalev P, Bergström J (2006) J Alloy Compd 421:166
11. Leong CC, Lu L, Fuh JYH, Wong YS (2002) Mater Sci Eng A338:81
12. Tan KH, Chua CK, Leong KF, Cheah CM, Cheang P, Abu Bakar MS, Cha SW (2003) Biomaterials 24:3115
13. Shishkovsky I, Yadroitsev I, Bertrand Ph, Smurov I (2007) Appl Surf Sci 254:966
14. Ramesha CS, Srinivas CK, Channabasappa BH (2009) Wear 267:1777
15. Vaucher S, Paraschivescu D, Andre C, Beffort O (2002) In: Materials week, 30.09.–2.10.2002, ICM-Munich, ISBN: 3-88355-314-X
16. Simchi A, Godlinski D (2008) Scripta Mater 59:199
17. Viala JC, Fortier P, Bouix J (1990) J Mater Sci 25:1842. doi:10.1007/BF01045395
18. Gacsi Z, Kovacs J, Pieczonka T, Buza G (2002) Surf Coat Technol 151–152:320
19. Kurtz W, Fischer DJ (1992) Fundamentals of solidification. Trans. Tech. Publications, Aedermannsdorf, Switzerland
20. Grabowski A, Nowak M, Sleziona J (2005) Opt Lasers Eng 43:233
21. Anandkumar R, Almeida A, Colaço R, Vilar R, Ocelik V, De Hosson J, Th M (2007) Surf Coat Technol 201:9497
22. Lee J-C, Byun J-Y, Oh C-S, Sek H-K, Lee H-I (1997) Acta Mater 45:5303